

Supplemental information

**Poly(ADP-ribosyl)ation enhances nucleosome
dynamics and organizes DNA damage repair
components within biomolecular condensates**

Michael L. Nosella, Tae Hun Kim, Shuya Kate Huang, Robert W. Harkness, Monica Goncalves, Alisia Pan, Maria Tereshchenko, Siavash Vahidi, John L. Rubinstein, Hyun O. Lee, Julie D. Forman-Kay, and Lewis E. Kay

1. Supplementary Figures

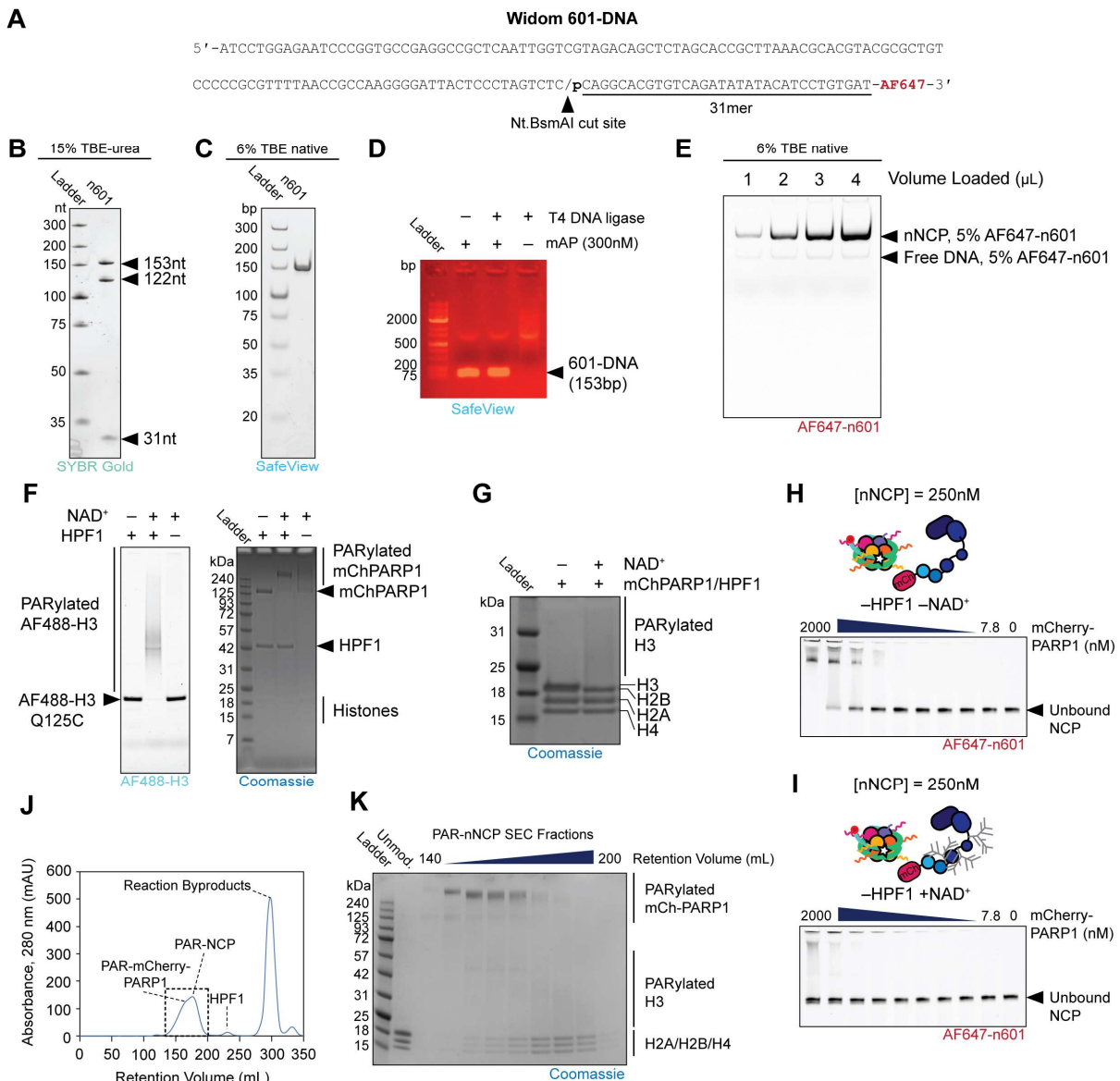


Figure S1. Preparation and modification of nucleosome core particle (NCP) samples; related to Figures 1-5 and STAR Methods. (A) Nucleotide sequence of Widom 601-DNA. The Nt.BsmAI excision site is indicated by a slash (/) within the restriction site: GTCTCN/N, where N is any nucleobase. In the 31nt sequence succeeding the excision site ('31mer'), the location of the 5' phosphate (p) and 3' AlexaFluor 647 label (-AF647) are indicated. (B) Denaturing TBE-urea 15% polyacrylamide gel resolving nicked, mAP-treated 601-DNA. Single-stranded DNA fragments are stained with SYBR Gold. Note the presence of three bands: a 153nt fragment corresponding to the unnicked strand, and 122nt and 31nt fragments corresponding to the nicked strand. (C) Native TBE 6% polyacrylamide gel of nicked, metagenomic alkaline phosphatase (mAP)-treated 601-DNA. A single double-stranded

DNA species corresponding to the full 601-DNA sequence (153nt) is stained with SafeView. (D) 1% agarose-TAE gel depicting products of a T4 ligation reaction including mAP-treated or untreated 601-DNA. Without mAP-treatment, DNA molecules are concatenated by the ligase and migrate as a distribution of high molecular weight species. With mAP-treatment, 601-DNA is impervious to ligation and travels as a single species between the 75bp and 150bp markers. (E) Native TBE 6% polyacrylamide gel depicting various concentrations of 5mol% AF647-labelled nicked 601-DNA-containing NCPs (nNCPs), along with small amounts of residual 'free' DNA. Species are visualized by fluorescence of the AF647 dye adjoined to the 31mer. (F) 4-12% polyacrylamide SDS gel resolving AF488-labelled H3(Q125C)-containing nNCPs PARylated by mChPARP1 in the presence or absence of HPF1. Both panels are the same gel imaged by AF488 fluorescence (*left*) or Coomassie staining (*right*). (G) Coomassie-stained 4-12% polyacrylamide SDS gel showing little change in mobility of H2A, H2B and H4 in the presence (+NAD⁺) or absence (–NAD⁺) of PARylation. Note that unmodified H2B and H3 bands are partially overlapping. (H) Electrophoretic mobility shift assays (EMSAs) involving unPARylated nNCPs and mChPARP1 at different concentrations of mChPARP1, as indicated. Samples are resolved on a native TBE 6% polyacrylamide gel and imaged by AF647 fluorescence of n601-DNA. (I) Same as (H) except mChPARP1 is automodified (20min, 37°C) by adding NAD⁺ prior to electrophoresis. Note that nNCPs are unmodified because HPF1 is absent. (J) Size exclusion chromatogram (SEC) of a nNCP PARylation reaction prepared for NMR and resolved on a HiLoad Superdex 200 26/60 column. Protein and DNA species are detected by UV absorbance at 280nm. (K) Coomassie-stained SDS-polyacrylamide gel resolving SEC fractions corresponding to the hatched box in (J). 'Unmod.' denotes an unmodified nNCP sample for comparison. Note that only three discrete histone bands appear in the modified samples because PARylated H3 migrates as a higher molecular weight smear. Fractions in the range of retention volumes ~150-200mL were typically collected for NMR samples.

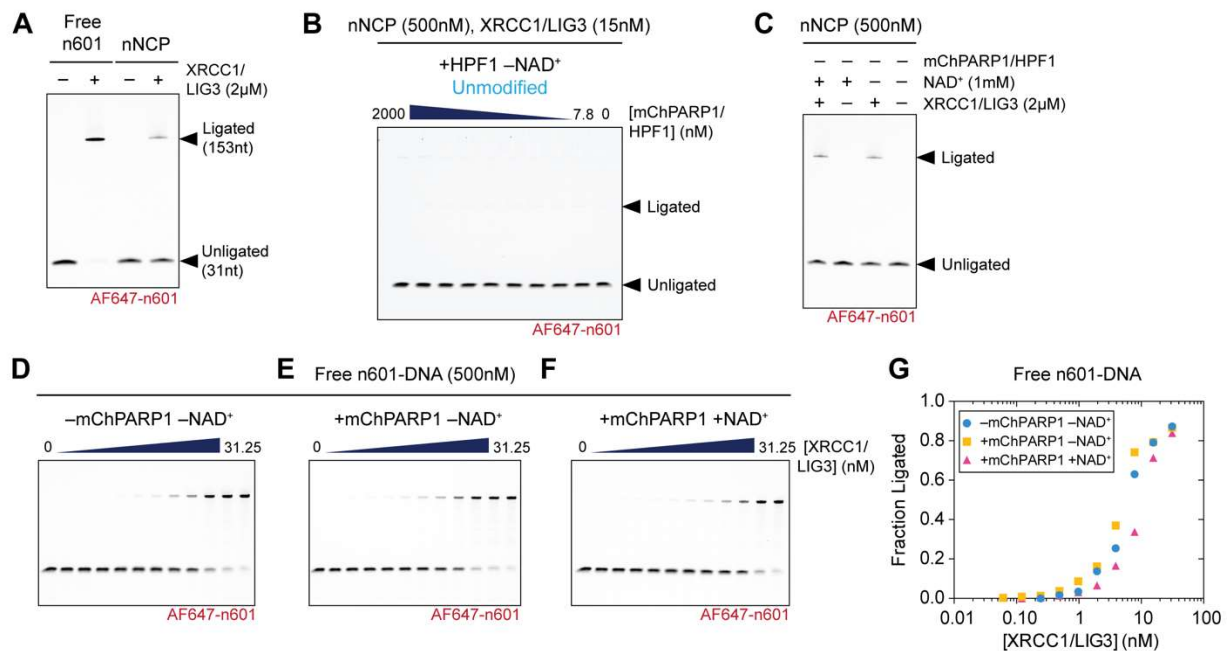


Figure S2. Supplementary ligase and micrococcal nuclease data; related to Figures 1 and 2. (A) Denaturing TBE-urea 15% polyacrylamide gel resolving the products of ligating 5mol% AF647-labelled n601-DNA ('free' n601) or nNCPs (both 500nM) with XRCC1/LIG3 (2μM). Note that at high concentrations of XRCC1/LIG3 (2μM) ligation is observed, while at lower concentrations (31nM) ligation cannot be quantified (Fig. 1C) in the absence of PARylation. (B) Products of ligating 5mol% AF647-labelled nNCPs (500nM) with XRCC1/LIG3 (15nM) in the presence of varying mChPARP1/HPF1 concentrations, but in the absence of NAD⁺. All molecules are unmodified. (C) Ligation of 5mol% AF647-labelled nNCPs (500nM) with XRCC1/LIG3 (2μM) in the presence or absence of NAD⁺ (1mM). mChPARP1/HPF1 was not present. At 2μM XRCC1/LIG3, small amounts of nNCP ligation occur without PARylation. (D) Ligation of 5mol% AF647-labelled n601-DNA (500nM) at various concentrations of XRCC/LIG3 in the absence of mChPARP1/HPF1 and NAD⁺. (E) Same as (D) with mChPARP1/HPF1 (1μM/1.5μM) present. (F) Same as (E) with mChPARP1/HPF1 and NAD⁺ (1mM) present to induce PARylation. (G) Quantification of results in (D-F).

calculated from spectra in (C). (E-G) $J(0)$ values calculated for H2A (E), H2B (F) and H4 (G) in PARylated (*red*) and unmodified (*black*) nNCPs, in 20mM sodium phosphate, 100mM NaCl, 1mM EDTA, pH 6.0.

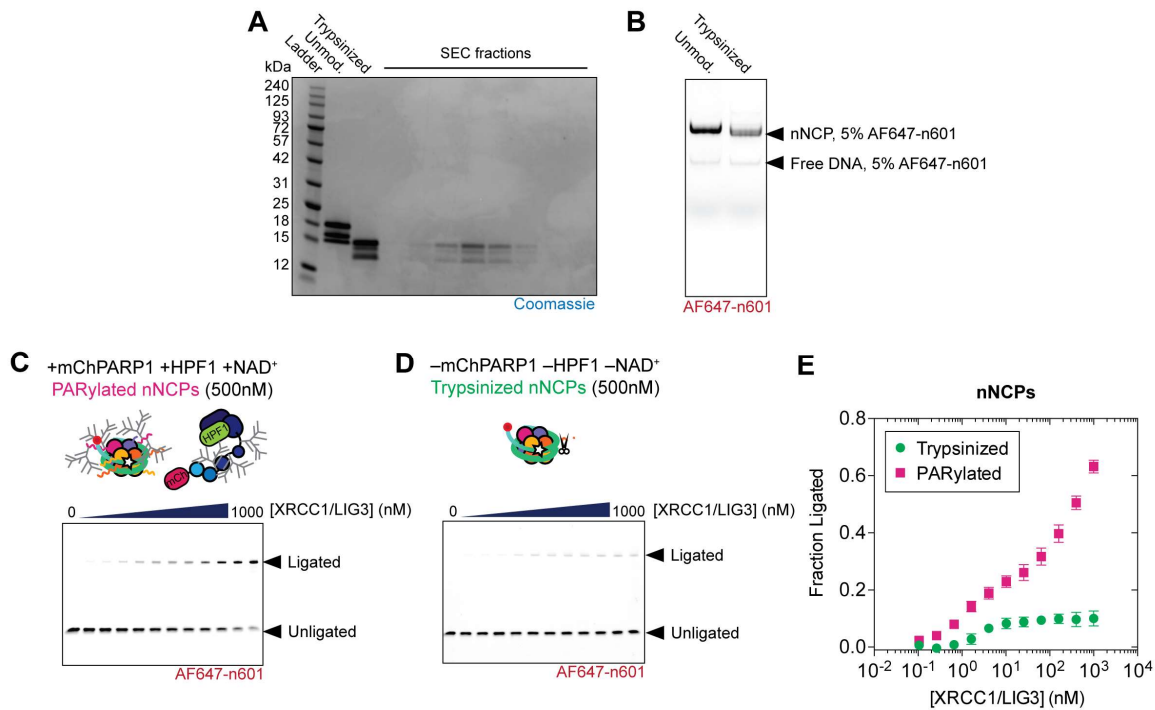


Figure S4. Preparation and ligation of trypsinized nNCPs; related to Figures 2,4 and 5. (A) Coomassie-stained SDS-polyacrylamide gel depicting fractions from size exclusion chromatography (SEC) of a trypsinized nNCP sample. ‘Unmod.’ denotes an untrypsinized sample; note how all four histone migrate more slowly compared to the trypsinized case. Trypsinized histones coelute, suggesting NCPs remain intact following tail removal. (B) Native TBE 6% polyacrylamide gel resolving unmodified (‘unmod.’) and trypsinized nNCPs containing 5mol% AF647-n601 DNA. (C) Ligation of PARylated, 5mol% AF647-labelled nNCPs (500nM) at XRCC1/LIG3 concentrations extending up to 1 μ M. (D) Ligation of trypsinized 5mol% AF647-labelled nNCPs (500nM) at various XRCC1/LIG3 concentrations and in the absence of mChPARP1/HPF1. (E) Quantification of results in (C) and (D) based on three independent replicates. Error bars represent standard deviation of the mean fraction ligated.

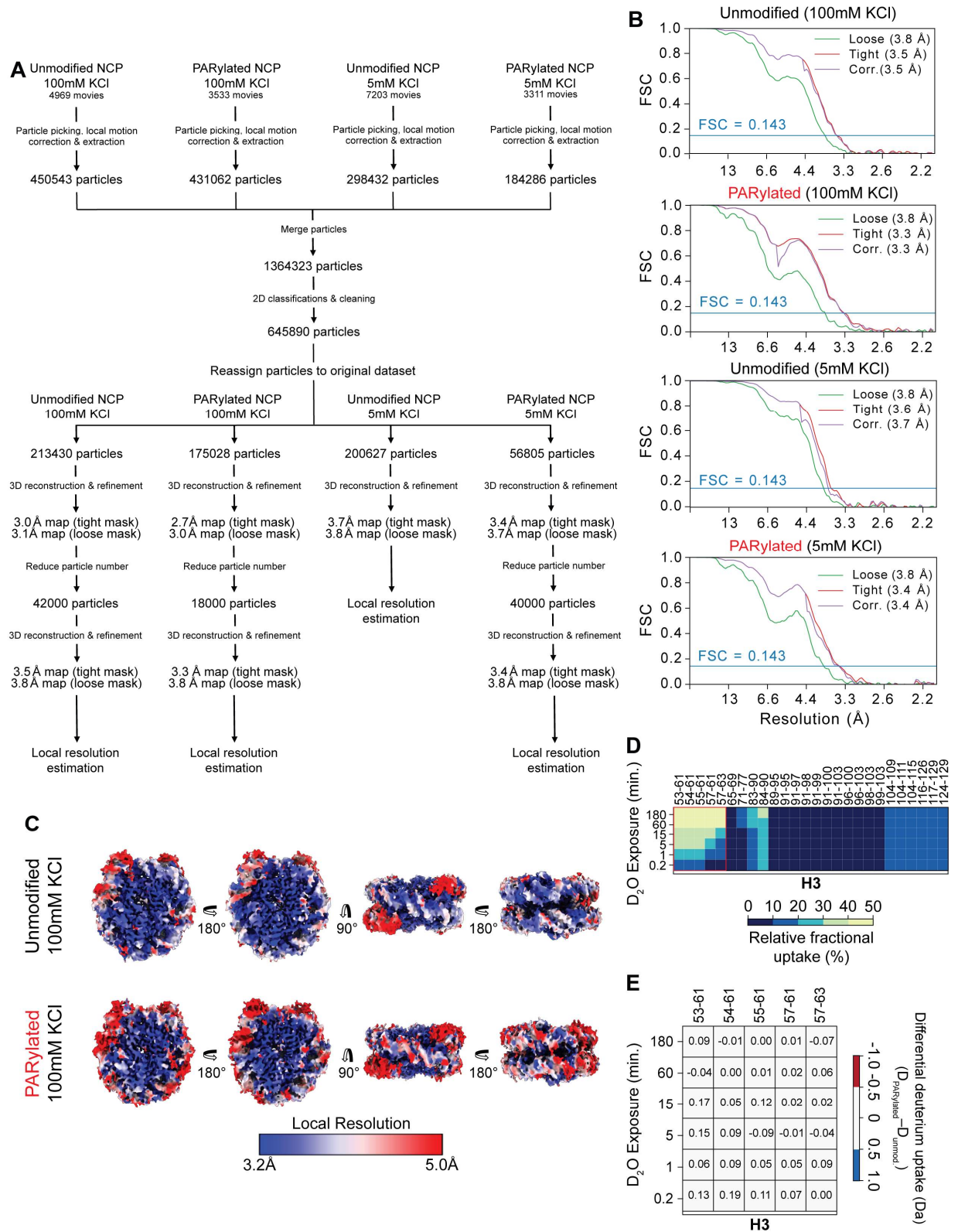


Figure S5. Characterization of DNA dynamics in unmodified and PARylated nNCPs by hydrogen-deuterium exchange mass spectrometry (HDXMS) and cryo-

EM local resolution analysis; related to Figure 3 and STAR Methods. (A) Flowchart summarizing processing and analysis workflow of cryo-EM data for local resolution analysis. Particles picked from datasets acquired from PARylated and unmodified nNCP samples at different KCl concentrations were merged for 2D classification. Following reassignment to the original datasets, particles were further analyzed by 3D reconstruction. In some datasets, the number of particles was limited to yield similar overall resolutions for the 3D density maps. (B) Plots of Fourier Shell Correlation (FSC) versus resolution (Å) for cryo-EM maps of each nNCP condition (unmodified or PARylated, 100mM or 0mM KCl). FSC curves were calculated after applying a loose mask (*green*; the density map thresholded at 50% of its maximum value and dilated 25Å with an additional 15Å cosine falloff), a tight mask (*red*), and the tight mask with the FSC corrected for the effect of masking (*corr.*, *violet*) [S1]. Using the standard CryoSPARC automatic procedure, the tight mask was tightened until FSC(0.143) was equal for the tight mask and the tight mask corrected for the effect of masking. Blue horizontal lines indicate FSC = 0.143. (C) Cryo-EM density maps of PARylated and unmodified nNCPs at 'high' salt: 20mM Tris-HCl, 100mM KCl, 0.1mM EDTA, pH 7.5. Maps are coloured by local resolution and four different views of the same map are shown: shades of blue indicate better resolution, shades of red indicate worse resolution. (D) Heatmap depicting relative fractional uptake values as a function of D₂O exposure time for peptides originating from H3 in unmodified or PARylated nNCPs. The red box highlights the set of peptides indicated in (E). (E) Differential deuterium uptake of select H3 peptides originating from unmodified and PARylated histones. Deuterium uptake for each peptide was calculated as a function of the duration of deuterium exposure, using $D(t) = \frac{m_t - m_0}{m_{100} - m_0}$, where m_t is the measured centroid mass of the peptide of interest at time t , and m_0 and m_{100} correspond to the measured centroid mass for the undeuterated control and the theoretical maximum deuteration, respectively (see Methods).

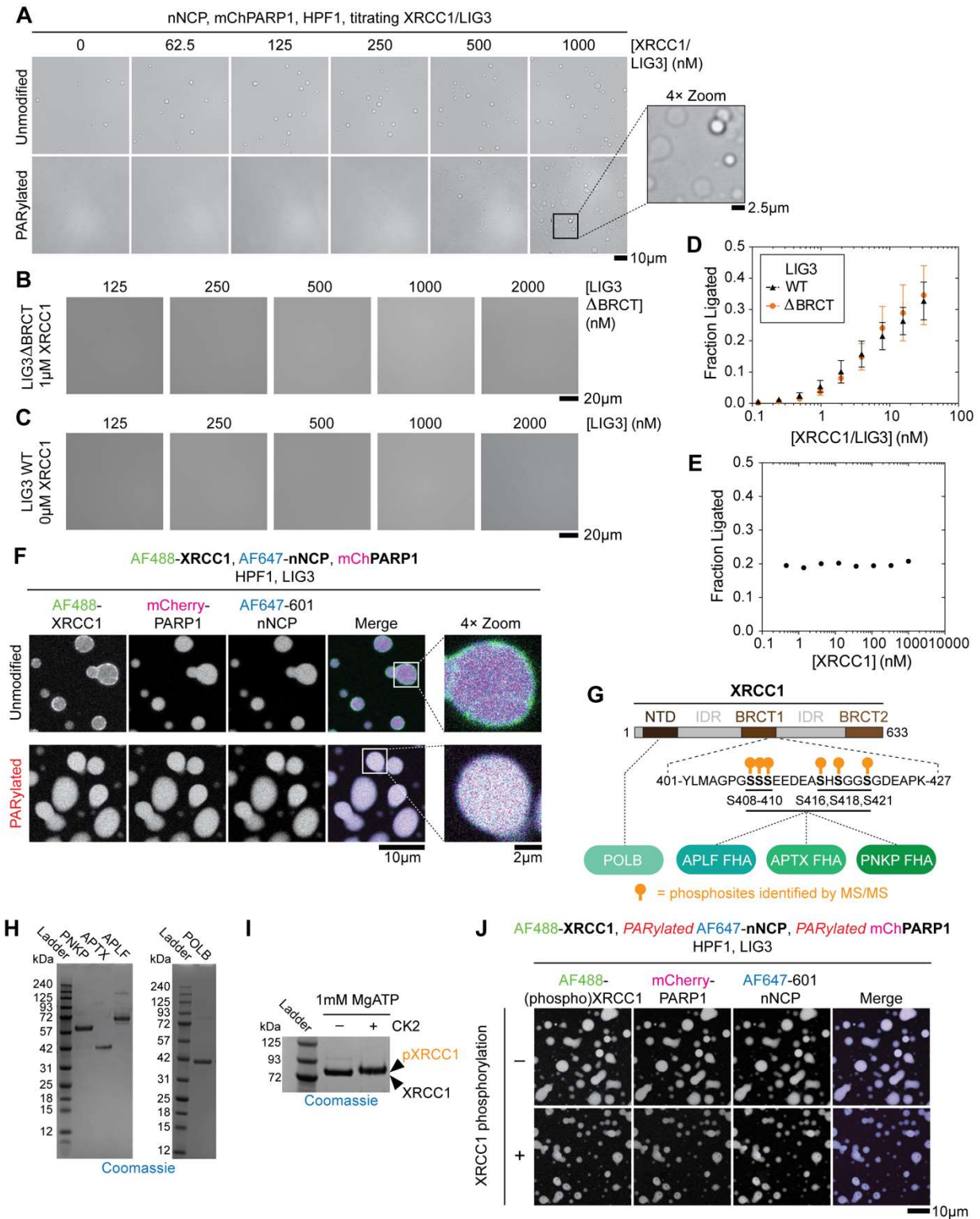


Figure S6. Supplementary condensate data, including effects of condensation on ligase activity and the effects of XRCC1 phosphorylation on condensate morphology; related to Figure 5. (A) Differential interference contrast (DIC)

micrographs of nNCP samples containing mChPARP1/HPF1 (1 μ M/1.5 μ M) and variable concentrations of XRCC1/LIG3, with or without PARylation. Micrographs including PARylation were contrast-adjusted to better highlight features. Scale bar: 10 μ m. (B) DIC micrographs of samples containing PARylated nNCPs (500nM), PARylated mChPARP1 (1 μ M), HPF1 (1.5 μ M), XRCC1 (1 μ M) and various concentrations of LIG3 Δ BRCT. Scale bar: 20 μ m. (C) DIC micrographs of samples containing PARylated nNCPs (500nM), PARylated mChPARP1 (1 μ M), no XRCC1 (0 μ M) and various concentrations of full length LIG3. Scale bar: 20 μ m. (D) Ligation of PARylated, 5mol% AF647-labelled nNCPs (500nM) in the presence of varying concentrations of XRCC1/LIG3 (black, full-length 'WT') and XRCC1/LIG3 Δ BRCT (orange). Error bars represent standard deviation of the mean from three independent replicate experiments. (E) Ligation of PARylated, 5mol% AF647-labelled nNCPs (500nM) in the presence of varying concentrations of XRCC1 and constant LIG3 (15nM). (F) Fluorescence micrographs of samples containing mChPARP1/HPF (1 μ M/1.5 μ M), partially AF488-labelled XRCC1 (1 μ M), LIG3 (1 μ M), with or without NAD⁺ (1mM) to induce PARylation. Scale bar: 10 μ m or 2 μ m (zoomed-in panels). (G) Schematic of the domain structure of XRCC1 and its interactions (hatched black lines) with DNA polymerase beta (POLB) and forkhead associated (FHA) domain-containing proteins, aprataxin- and PNK-like factor (APLF), aprataxin (APTX), and polynucleotide kinase 3'-phosphatase (PNKP). These selections were rationalized by their known interaction properties: APLF, APTX and PNKP bind PAR [S2, 3] and XRCC1 (G408-S421) especially in its CK2-phosphorylated state (see G) [S4, 5]; POLB interacts with the XRCC1 N-terminal domain (NTD) via a dedicated interface that is unaffected by CK2-phosphorylation [S6, 7]. We predicted that these proteins' interactions with PAR and/or phospho-XRCC1 would dictate the extent to which they partition into nNCP condensates. Orange marks represent *in vitro* CK2-phosphorylation sites identified by tandem mass spectrometry. A subset of the *in vitro* phosphorylation sites matched those previously identified in endogenous XRCC1 [S4]. (H) Coomassie-stained SDS-polyacrylamide gels depicting purified, recombinant APLF, APTX, PNKP (*left*) and POLB (*right*). (I) Coomassie-stained SDS-polyacrylamide gel showing diminished migration of XRCC1 following phosphorylation with casein kinase 2 (CK2) and 1mM MgATP. (J) Fluorescence micrographs of samples containing partially AF488-labelled XRCC1 (either unmodified or CK2-phosphorylated, including the dye-labelled fraction; 1 μ M), LIG3 (1 μ M), PARylated mChPARP1/HPF1 (1 μ M/1.5 μ M) and PARylated 5mol% AF647-labelled nNCPs (500nM). CK2-phosphorylation did not change the overall morphological characteristics of the droplets, nor did it affect the localization of AF488-XRCC1, mChPARP1 and AF647-nNCPs in the presence of PARylation. Scale bar: 10 μ m.

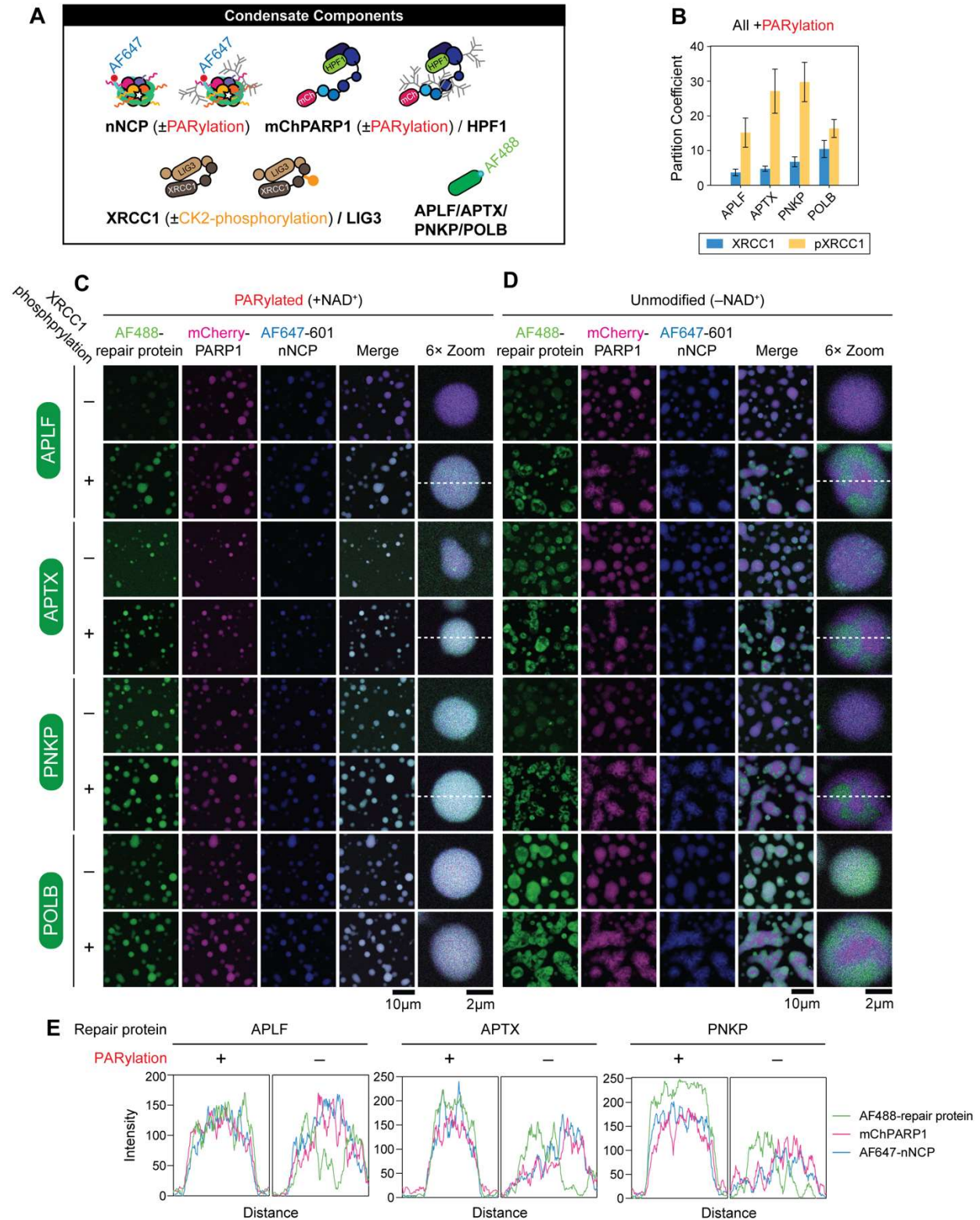


Figure S7. PARylation and XRCC1 phosphorylation regulate enrichment and localization of APLF, APTX, PNKP and POLB in nNCP condensates; related to Figure 5. (A) Graphic illustration of condensate components with potential labelling

schemes and PTMs. (B) Partition coefficients calculated from fluorescence signals measured in PARylated samples containing each indicated AF488-labelled repair protein. Overall, these proteins' partition coefficients correlated with their propensities to interact with XRCC1 in its unmodified or CK2-phosphorylated states. APLF, APTX and PNKP, which all engage in phospho-specific interactions with XRCC1, were especially enriched in condensates containing CK2-phosphorylated XRCC1 and PARylated NCPs, whereas POLB partitioned strongly into condensates containing unmodified or phosphorylated XRCC1, likely because it binds XRCC1 in a phosphorylation-independent manner. pXRCC1: CK2-phosphorylated XRCC1. Error bars represent standard deviation from three independent experiments. (C) Fluorescence micrographs of PARylated nNCP samples containing different, partially AF488-labelled DNA repair proteins. All samples contain XRCC1/LIG3 (1 μ M) and PARylated mChPARP1/HPF1 (1 μ M/1.5 μ M). XRCC1 was unmodified or CK2-phosphorylated in each sample. PARylation promoted homogenous mixing of all components into a single condensed phase. Scale bar: 10 μ m or 2 μ m (zoomed-in panels). (D) Same as (C) except in the absence of PARylation. In the presence of phosphorylated XRCC1, APLF, APTX and PNKP partitioned into condensate subcompartments that were distinct from the mChPARP1- and nNCP-enriched phase, similar to what was observed for AF488-labelled LIG3 and XRCC1 in the absence of PARylation (Fig. 5C,S6F). When both PARylation and XRCC1-phosphorylation were excluded, none of the repair proteins—except for POLB, which interacts with XRCC1 regardless—partitioned strongly into the condensates, likely due to the dual loss of interactions with PAR and XRCC1. Scale bar: 10 μ m or 2 μ m (zoomed-in panels). (E) Plots depicting fluorescence intensities measured along the hatched white lines indicated in the corresponding merged images of APLF, APTX or PNKP-containing droplets in (C) and (D).

2. SI References

- S1. Chen, S., et al. (2013) High-resolution noise substitution to measure overfitting and validate resolution in 3D structure determination by single particle electron cryomicroscopy. *Ultramicroscopy*, 2013. **135**: 24-35. 10.1016/j.ultramic.2013.06.004
- S2. Li, M., et al. (2013) The FHA and BRCT domains recognize ADP-ribosylation during DNA damage response. *Genes Dev*, 2013. **27**(16): 1752-68. 10.1101/gad.226357.113
- S3. Ahel, I., et al. (2008) Poly(ADP-ribose)-binding zinc finger motifs in DNA repair/checkpoint proteins. *Nature*, 2008. **451**(7174): 81-5. 10.1038/nature06420
- S4. Loizou, J.I., et al. (2004) The protein kinase CK2 facilitates repair of chromosomal DNA single-strand breaks. *Cell*, 2004. **117**: 17-28. 10.1016/s0092-8674(04)00206-5
- S5. Caldecott, K.W. (2019) XRCC1 protein; Form and function. *DNA Repair (Amst)*, 2019. **81**: 102664. 10.1016/j.dnarep.2019.102664
- S6. Kubota, Y., et al. (1996) Reconstitution of DNA base excision-repair with purified human proteins: interaction between DNA polymerase beta and the XRCC1 protein. *The EMBO Journal*, 1996. **15**(23): 6662-6670. 10.1002/j.1460-2075.1996.tb01056.x
- S7. Dianova, II, et al. (2004) XRCC1-DNA polymerase beta interaction is required for efficient base excision repair. *Nucleic Acids Res*, 2004. **32**(8): 2550-5. 10.1093/nar/gkh567